SCIENCE CHINA
Chemistry

• ARTICLES •

December 2015 Vol.58 No.12: 1918–1928
doi: 10.1007/s11426-015-5446-2

Numerical simulation of CO_2-ionic liquid flow in a stirred tank

Zailong Ouyang[1,2], Di Bao[1,2], Xin Zhang[1,2], Haifeng Dong[1], Ruiyi Yan[1], Xiangping Zhang[1*] & Suojiang Zhang[1*]

[1]*Beijing Key Laboratory of Ionic Liquids Clean Processing; State Key Laboratory of Multiphase Complex Systems; Institute of Process Engineering, Chinese Academy of Sciences, Beijing 100190, China*
[2]*College of Chemistry and Chemical Engineering, University of Chinese Academy of Sciences, Beijing 100049, China*

Received January 23, 2015; accepted March 26, 2015; published online July 24, 2015

Ionic liquids (ILs) are new solvents that represent a breakthrough for absorption and conversion of CO_2. However, there has been little research on the hydrodynamics of gas-IL systems in stirred tanks, and this has become a bottleneck for development of IL-based reactors. In the present study, a CO_2-IL ([bmim][BF_4]) flow in a stirred tank was studied using computational fluid dynamics (CFD). A new drag coefficient model that is specific to a gas-ionic liquid system and a population balance model (PBM) were adopted to describe the bubble behavior, such as gas holdup and bubble size evolution, precisely. The predicted results for the total gas holdup and local Sauter diameter agree well with the experimental data. The influences of the gassing rate, agitation speed, and temperature on local gas holdup, bubble size distribution, and interfacial area for the CO_2-[bmim][BF_4] system were also investigated. The results of this study provide fundamental information for designing gas-IL systems for stirred tanks.

multiphase flow, ionic liquids, carbon dioxide, stirred tank, computational fluid dynamics, population balance model

1 Introduction

Ionic liquids (ILs) are novel media that have some unique properties, including negligible vapor pressure, high thermal stability, and the possibility of structure modification. Because of these unique properties of ILs, many researchers have studied their potential applications, such as synthesis, catalysis, electrolysis, and separation, in detail [1–3]. In industries, large amounts of CO_2 emissions in exhaust flue gas have been proven to be the cause of the serious global warming problem. To address this situation, various types of absorbents have been developed for use in CO_2 capture. Compared with conventional absorbents used in exhaust flue treatment, ILs have been shown to have higher solubility and require less energy for regeneration [4–6]. Furthermore, ILs can play important roles in reactions, especially in the conversion of CO_2 into chemicals and fuels. Zhang *et al.* [7] found that formic acid can be easily synthesized from CO_2 and H_2O by the addition of an amine-functionalized basic IL ([DAMI][Tfo]). Sun *et al.* [8,9] focused on producing cyclic carbonates from CO_2 and achieved efficient reactivity and high selectivity in the presence of hydroxyl-functionalized IL as the homogeneous catalyst. ILs have also been found to be attractive alternatives to traditional solvents for use in CO_2 conversion to alcohols [10].

As the above-mentioned research findings indicate, ILs have shown significant potential for use in industrial processes. However, the high viscosity and low CO_2 diffusivity of most ILs lead to high resistance to gas-liquid flow and mass transfer, which are very important issues in reactor design. Stirred tanks are widely used in chemical industries to provide excellent mixing ability and high-quality gas dispersion for processes involving chemical reactions. Experimental techniques have been widely used to investigate the hydrodynamics in reactors. In previous research, we

*Corresponding authors (email: xpzhang@ipe.ac.cn; sjzhang@home.ipe.ac.cn)

conducted a series of experiments, coupled with a high-speed image pick-up method [11–13], to examine the bubble behavior in ILs in a bubble column. We proposed a drag correlation and presented the gas holdup and bubble size distribution in detail. Kaji *et al.* [14] used high-speed video and conductivity to compare the bubble behavior of ILs and conventional molecular solvents by examining the differences in the flow pattern characteristics of air-ILs and air-glycerol systems in a bubble column. Torres-Martínez *et al.* [15] conducted research on IL drop dispersion using optical reflectance measurement in a three-phase (gas-water-IL) stirred bioreactor. However, the hydrodynamics related to the flow pattern and bubbles in a stirred tank involving an IL system were not investigated.

Although knowledge of the phenomena and some correlations have been used to characterize multiphase behavior in the above-mentioned experiments, the detailed physics involved have still not been thoroughly described for a wide range of experimental conditions. The computational fluid dynamics (CFD) method can be used to overcome the limitations of previous experiments in an efficient manner and can provide insight into the transportation phenomena that occur in reactors. To describe the flow pattern and bubble behavior in a stirred tank, some particular aspects should be considered. For example, in some previous studies [16–18], the Eulerian-Eulerian method has been employed to describe flow patterns and local gas holdup, assuming a constant bubble size, and has been proven to be a very promising method. With respect to the important issue of the treatment of turbulence, models that employ direct numerical simulation (DNS) and large-eddy simulation (LES) have been shown to provide accurate predictions [19,20], but the computational costs associated with these methods are enormous. The Reynolds-averaged Navier-Stokes approach offers a good tradeoff between acceptable results and computational costs. Additionally, the assumption of constant bubble size cannot account fully for the inhomogeneity of gas-liquid reactors. Lane *et al.* [21] and Kerdouss *et al.* [22] employed a population bubble density model (BDM), based on a bubble number density equation, to predict the local average bubble size in stirred tanks, and found that the CFD-BDM method resulted in acceptable predictions. To make the method more efficient in application to complex processes, in which bubble breakage and coalescence have significant impacts on the hydrodynamics, many researchers have applied a full population balance model (PBM), in which the bubble size represents the internal coordinate [23–25]. At the same time, attention has been focused on methods for solving the population balance equation (PBE). The class method (CM), which discretizes the particle population into a finite number of size intervals, is particularly useful when dealing with crystal processes [26]. However, the disadvantage of the CM is that it is computationally expensive if a large number of intervals are needed. McGraw [27] proposed the quadrature method of moments (QMOM) for modeling aerosol evolution and coagulation problems. Marchisio *et al*. [28,29] implemented the method for aggregation and breakage processes, and the results showed that the method requires a relatively small number of scalar equations to track the moments of population with a small error. As described above, numerical strategies can also be suitable for simulations of gas-IL systems in stirred tanks. However, apart from the work of Wang *et al*. [30,31], who applied improved CFD models to the study of single bubble deformation and the multi-bubble process of absorbing CO_2 with ionic liquids in a small bubble column, little research on numerical simulation of gas-IL systems has been conducted.

In the present study, a stirred tank agitated via a single Rushton turbine was set up for experimental operation. A high-speed pick-up system was used to capture bubble dispersion at various measuring positions. A Eulerian multiphase model, coupled with a PBM, was employed to study the flow pattern and bubble behavior. The computational results were validated by comparison with the experimental data, and information on the influences of various operating conditions on the gas holdup, Sauter diameter (d_{32}), volumetric bubble distribution, and local interfacial area was gathered.

2 Methodology

2.1 Modeling of multiphase fluid dynamics

The gas-liquid fluid dynamics are described by the Eulerian-Eulerian two-fluid model, in which the gas and liquid phases are treated as different continua, each penetrating into the other. The Reynolds-averaged method was used for the mass and momentum balance equations. The volume fraction (α_i) equation takes the following specific form:

$$\frac{\partial}{\partial t}\left(\alpha_i\rho_i\right)+\nabla\cdot\left(\alpha_i\rho_i\boldsymbol{U}_i\right)=S_i \tag{1}$$

where $\boldsymbol{U}_i$ and ρ_i denote the mean velocity and density, respectively, of phase i (gas or liquid), S_i is the source term (kg/(m^3 s)). We propose the assumption that no mass flux (S_i=0) exists between the gas and liquid phases.

The momentum conservation equation can be expressed as follows:

$$\frac{\partial}{\partial t}\left(\alpha_i\rho_i\boldsymbol{U}_i\right)+\nabla\cdot\left(\alpha_i\rho_i\boldsymbol{U}_i\boldsymbol{U}_i\right) = -\alpha_i\nabla p+\alpha_i\rho_i\boldsymbol{g}+\nabla\cdot\bar{\bar{\boldsymbol{\tau}}}_i+\boldsymbol{F}_i \tag{2}$$

where p is the pressure shared by the two phases in any computational domain, $\bar{\bar{\boldsymbol{\tau}}}$ is the phase stress-strain tensor (kg/(m s^2)), and $\boldsymbol{F}_i$ accounts for interphase exchanges (N/m^3), including the drag force, virtual mass force, and lift

force. In the present study, the drag force was considered to be the dominant term to be taken into account in analysis of the gas-liquid behavior in a stirred tank. This approach has proven to yield acceptable predictions in other studies [16,24]. The specific form of the equation for the drag force is as follows:

$$\boldsymbol{F}_{\mathrm{cd}} = \frac{3}{4}\rho_{\mathrm{c}}\alpha_{\mathrm{b}}\frac{C_{\mathrm{D}}}{d_{\mathrm{b}}}\left|\boldsymbol{U}_{\mathrm{b}}-\boldsymbol{U}_{\mathrm{c}}\right|\left(\boldsymbol{U}_{\mathrm{b}}-\boldsymbol{U}_{\mathrm{c}}\right) \tag{3}$$

where $\boldsymbol{F}_{\mathrm{cd}}$ is the drag force (N/m^3), α_{b} is the volume fraction of gas phase, ρ_{c} is the density of liquid phase, C_{D} is the drag coefficient, d_{b} is the bubble diameter (m), $\boldsymbol{U}_{\mathrm{b}}$ is the time-averaged velocity of gas phase (m/s), $\boldsymbol{U}_{\mathrm{c}}$ is the time-averaged velocity of liquid phase (m/s). The correlation proposed by Dong *et al*. [13], which is a function of the Reynolds number and the Morton number, is used to describe the CO_2-ILs system:

$$C_{\mathrm{D}} = \begin{cases} 22.73Re^{-0.849}Mo^{0.020}, & 0.5 \leqslant Re \leqslant 5 \\ 20.08Re^{-0.636}Mo^{0.046}, & 5 \leqslant Re \leqslant 50 \end{cases} \tag{4}$$

$$Re = \frac{\rho_{\mathrm{c}}\left|\boldsymbol{U}_{\mathrm{b}}-\boldsymbol{U}_{\mathrm{c}}\right|d_{\mathrm{b}}}{\mu_{\mathrm{c}}} \tag{5}$$

$$Mo = \frac{g\mu^4\left(\rho_{\mathrm{c}}-\rho_{\mathrm{b}}\right)}{\sigma^3{\rho_{\mathrm{c}}}^2} \tag{6}$$

where Re is the Reynolds number, Mo is the Morton number, ρ_{b} is the density of gas phase, g is the gravitational acceleration (m/s^2), μ is the viscosity (Pa s).

Several empirical correlations have been developed for isolated bubbles in stagnant liquids. The effect of reduction in the slip velocity of bubbles due to turbulence should also be considered. By observing the ratio changes between bubble diameter and the Kolmogorov microscale (λ), Brucato *et al*. [32] developed an expression for the turbulent drag factor based on particle settling measurements:

$$\frac{C_{\mathrm{Df}}-C_{\mathrm{D}}}{C_{\mathrm{D}}} = 8.76\times10^{-4}\left(\frac{d_{\mathrm{b}}}{\lambda}\right)^3 \tag{7}$$

where C_{Df} is the modified drag coefficient, λ is the bubble size (m).

The standard k-ε mixture model is applied to capture the important features of the gas-liquid flow, and the transport equations for the turbulent quantities are as follows:

$$\frac{\partial}{\partial t}\left(\rho_{\mathrm{m}}k\right)+\nabla\cdot\left(\rho_{\mathrm{m}}\boldsymbol{U}_{\mathrm{m}}k\right) = \nabla\cdot\left(\frac{\mu_t}{\sigma_k}\nabla k\right)+G_k-\rho_{\mathrm{m}}\varepsilon \tag{8}$$

$$\begin{aligned}&\frac{\partial}{\partial t}\left(\rho_{\mathrm{m}}\varepsilon\right)+\nabla\cdot\left(\rho_{\mathrm{m}}\boldsymbol{U}_{\mathrm{m}}\varepsilon\right)\\ &=\nabla\cdot\left(\frac{\mu_t}{\sigma_\varepsilon}\nabla\varepsilon\right)+\frac{\varepsilon}{k}\left(C_{1\varepsilon}G_k-C_{2\varepsilon}\rho_{\mathrm{m}}\varepsilon\right)\end{aligned} \tag{9}$$

where k is the turbulent kinetic energy (m^2/s^2), $\boldsymbol{U}_{\mathrm{m}}$ is the time-averaged velocity of mixture (m/s), ε is the turbulent dissipation rate (m^2/s^3), G_k represents the production of turbulence kinetic energy (kg/(m s^3)), σ_k and σ_ε are the constants of the turbulent model, $C_{1\varepsilon}$ and $C_{2\varepsilon}$ are the constants of the turbulent model. The turbulent viscosity of the mixture is determined from the following equation:

$$\mu_{t,\mathrm{m}} = \rho_{\mathrm{m}}C_\mu\frac{k^2}{\varepsilon} \tag{10}$$

The values of the constants in the equations are C_μ=0.09, $C_{1\varepsilon}$=1.44, $C_{2\varepsilon}$=1.92, σ_k=1.0, and σ_ε=1.3.

2.2 Population balance modeling

As described in the monograph written by Marchisio and Fox [33], the population balance equation (PBE) can be derived from a number density function (NDF). The NDF is characterized by two parts, one of which is the set of external coordinates that denote the spatial positions of the bubbles, and the other of which is the set of internal coordinates, including bubble size and composition. For our present case, the bubble size was represented by a single variable for the internal coordinates. Thus, the PBE could be expressed as follows:

$$\begin{aligned}&\frac{\partial n(L)}{\partial t}+\nabla\cdot\left(n(L)\boldsymbol{U}_{\mathrm{b}}\right)\\ &=\int_L^\infty\beta(L,\lambda)g(L,\lambda)n(\lambda)\mathrm{d}\lambda\\ &+\frac{1}{2}\int_0^\infty h\left(\left(L^3-\lambda^3\right)^{\frac{1}{3}},\lambda\right)n\left(\left(L^3-\lambda^3\right)^{1/3}\right)n(\lambda)\mathrm{d}\lambda\\ &-\frac{1}{2}\int_0^\infty h(L,\lambda)n(L)n(\lambda)\mathrm{d}\lambda-g(L)n(L)\end{aligned} \tag{11}$$

where $\boldsymbol{U}_{\mathrm{b}}$ is the bubble velocity and the terms on the right-hand side of Eq. (11) represent bubble birth and death rates due to coalescence and breakage; the breakage kernel $g(L)$ denotes the breakage frequency, $n(L)$ is the bubble number density function (m^{-4}), and $\beta(L,\lambda)$ is the probability density function (PDF) of bubbles breaking from size λ to size L; $h(L,\lambda)$ represents the coalescence kernel (m^3/s), which reflects two quantities: the frequency of coalescence of two bubbles of size L and λ, and the efficiency of aggregation.

It should be noted that the kernels for coalescence and breakage are derived from realistically physical objects. Therefore, various kernel models have been proposed for various conditions. Luo and Svendsen [34] developed a breakage kernel that encompassed both the breakage frequency and the PDF of breaking bubbles. The expression is written as follows:

$$\Omega(L,\lambda)=c_{\mathrm{B}}\left(1-\alpha_g\right)n\left(\frac{\varepsilon}{L^2}\right)^{1/3}\times\int_{\xi_{\min}}^{1}\frac{\left(1+\xi\right)^2}{\xi^{11/3}}\exp\left(-\frac{12c_{\mathrm{f}}\sigma}{\beta\rho_{\mathrm{c}}\varepsilon^{2/3}L^{5/3}\xi^{11/3}}\right)\mathrm{d}\xi \quad (12)$$

where σ is the surface tension (N/s). By integration over the size of eddies λ hitting bubbles of diameter L, the daughter bubble size distribution can be calculated directly from the model. For binary breakage, the coefficient of surface area increase, c_{f}, is taken to be equal to 0.26. ξ is the dimensionless eddy size with respect to $\xi=\lambda_{\mathrm{e}}/L$.

To describe the influence of turbulent fluctuations on bubble aggregation, the model derived from Coulaloglou and Tavlarides [35] was applied for the coalescence kernel:

$$h(\lambda,L)=C_1\varepsilon^{1/3}\left(\lambda+L\right)^2\left(\lambda^{2/3}+L^{2/3}\right)^{1/2}\eta(\lambda,L) \quad (13)$$

where $\eta(\lambda,L)$ represents the coalescence efficiency. According to Prince and Blanch [36], the coalescence efficiency can be expressed as follows:

$$\eta(\lambda,L)=\exp\left(-C_2\frac{\rho_{\mathrm{c}}^{1/2}\varepsilon^{1/2}}{\left(1/\lambda+1/L\right)^{5/6}\sigma^{1/2}}\right) \quad (14)$$

As described above, the adjustable constants C_1=1.0 and C_2=1.95 relate to the balance between coalescence rates and coalescence efficiencies for various research systems. In this study, in which a wide range of operating conditions were considered for a CO_2-[bmim][BF_4] system, the modified C-T model is more suitable because of the high-viscosity liquid phase.

The change in bubble size due to absorption between CO_2 and [bmim][BF_4] was considered to be negligible in this study. At 303 K, Henry's constant in [bmim][BF_4] is 6.16 MPa [37], and the mass transfer coefficient is in the range of 0.75×10^{-5} to 1.39×10^{-5} m/s [38]. Therefore, the rate of change for every single bubble size at 1 atm can be expressed as follows:

$$\frac{\partial d_{\mathrm{b}}}{\partial t}=\frac{2M_{\mathrm{g}}k_L\left(c_{\mathrm{i}}-c_0\right)}{\rho_{\mathrm{l}}} \quad (15)$$

where M_{g} is the molar mass of CO_2, c_{i} is the interfacial concentration of CO_2, and c_0 is equal to 0 for the initial conditions. Based on Eq. (15), the value of $\partial d_{\mathrm{b}}/\partial t$ was determined ranging from 4.80×10^{-8} to 8.90×10^{-8} m/s, which demonstrates that mass transfer between the gas and liquid phases exerts a negligible effect on the change in bubble size.

2.3 Solution method for the PBM

In the present study, the QMOM was selected as the solution method for the PBE. The quadrature approximation of the generic k^{th} moment, in terms of BSD, can be expressed as follows:

$$m_k=\int_0^\infty L^k n(L)\mathrm{d}L\approx\sum_{i=1}^{N}w_iL_i^{\,k} \quad (16)$$

where m_k is the moment of order k, N is the order of quadrature approximation defined by the N weights w_i and N abscissas L_i. The values of these variables can be calculated as the first $2N$ moments, using algorithms such as the product-difference algorithm proposed by Gordon [39], a detailed description of which is given by Marchisio *et al.* [29]. It is usually adequate to set N=3 to obtain accurate results. Thus, the six moments m_0, m_1, m_2, m_3, m_4, and m_5 are tracked. Some of the moments correspond to population properties. For example, the Sauter diameter, d_{32}, which is commonly used as the mean bubble size, is equal to the ratio between m_3 and m_2:

$$d_{32}=\frac{m_3}{m_2}=\frac{\int_0^\infty n(L)L^3\mathrm{d}L}{\int_0^\infty n(L)L^2\mathrm{d}L} \quad (17)$$

The transportation equation of moments is given by the following expression:

$$\frac{\partial m_k}{\partial t}+\nabla\cdot\left(\boldsymbol{U}_k m_k\right)=\frac{1}{2}\sum_{i=1}^{N}w_i\sum_{j=1}^{N}w_j\left(L_i^{\,3}+L_j^{\,3}\right)^{k/3}h\left(L_i,L_j\right)-\sum_{i=1}^{N}L_i^{\,k}w_i\sum_{j=1}^{N}w_jh\left(L_i,L_j\right)+\sum_{j=1}^{N}w_jg\left(L_i\right)\bar{b}_i^{(k)}-\sum_{j=1}^{N}w_jL_i^{\,k}g\left(L_i\right) \quad (18)$$

where

$$\bar{b}_k=\int_0^\infty L^k\beta\left(L,L_i\right)\mathrm{d}L \quad (19)$$

2.4 Grid independence

Four hexahedral grids with numbers of cells ranging from 18408 to 808921 were chosen for use in grid independence tests. The turbulent kinetic energy, which is an important parameter in evaluation of the quality of the stirred tank, was monitored. As shown in Figure 1, the turbulent kinetic energy increases considerably in the rotational region, whereas in the bulk region, the turbulent kinetic energy seems to be constant regardless of the grid resolution. The results also show that the maximum value of the turbulent kinetic energy increases with increasing grid refinement. However, when the number of grids was greater than that of grid3 (385888 cells), the monitoring values remained the same. Therefore, grid3 was adopted as the most suitable mesh for use in simulation in this study.

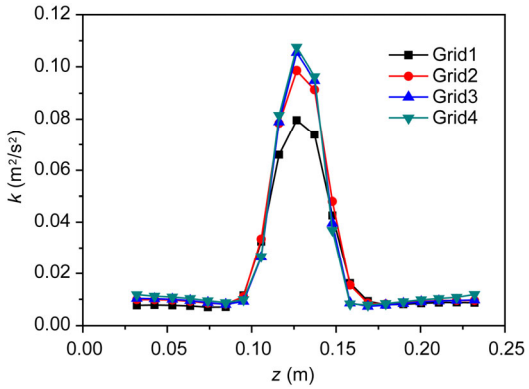

Figure 1 Values of turbulent kinetic energy for different grids along the axis direction (r=126 mm).

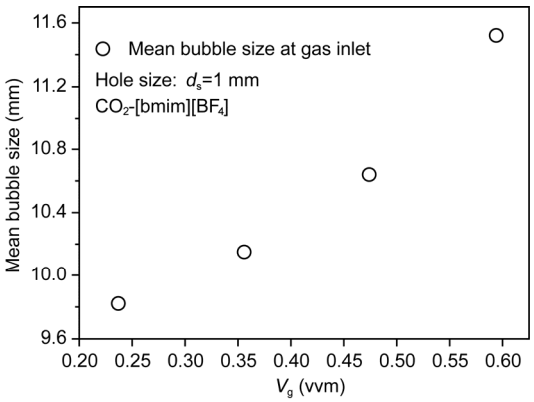

Figure 2 Measured mean bubble size at the gas inlet for different gassing rates.

2.5 Numerical strategy and boundary conditions

The stirred tank with a single impeller described in the next section was simulated. The physical properties of the liquid phase used in the simulations are reported in Table 1. Under various operating conditions (agitation speeds of 250–350 r/min, gas flow rates of 0.237–0.594 vvm, and temperatures of 292–330 K), a multiple reference frame (MRF) was adopted to model the motion of the impeller, and the spatial discretization for equations was resorted to the first-order upwind scheme. A computational domain of 385888 hexahedral cells was adopted based on the results of the grid independence tests. The flow field of the continuous phase was initially obtained using a steady-state solution. The PBM model was then employed to calculate the bubble size distribution, while the gas phase was introduced from the ring sparger. With respect to the boundary conditions, the magnitudes of the gas rates were equal to the experimental conditions. A normal distribution was assumed for the bubble size at the velocity inlet, with a measured mean bubble size (Figure 2) and a standard deviation of $0.16d_{32}$ [23]. Ten photos were taken at 1000 fps and a resolution of 1280 ×1024 pixels using a high-speed video camera, at various gas flow rates. These pictures were analyzed with image processing software to determine the values of significant bubble geometry parameters. The equivalent diameter of a sphere with the same volume as an ellipsoid was calculated from the following equation (a graphical illustration is shown in Figure 2 in the work of Dong *et al.* [13]):

Table 1 Physical properties of the liquid phase

T (K)	[bmim][BF_4]		
	σ (mN/m)	μ_c (mPa s)	ρ_c (g/mL)
292	44.9	94.1	1.202
310 [a)]	42.8	60.4	1.194
320 [a)]	42.3	39.9	1.187
330 [a)]	41.7	27.9	1.180

a) From Dong *et al.* [13].

$$d_e = \sqrt[3]{d_{b,max}^2 d_{b,min}} \quad (20)$$

The upper surface of the liquid was defined as a degassing boundary from which dispersed gas bubbles are allowed to escape but the continuous phase is not. Moreover, the convergence criteria for all transport equations were set to 10^{-3}, and the mass balance between the gas inlet and outlet was used as another criterion (relative deviation ⩽0.11%) to make a reasonable judgment concerning process convergence.

3 Experimental

3.1 Experimental procedure

The apparatus used in the experiments, shown in Figure 3, was a full-baffled, flat-bottomed cylindrical tank with an inner diameter of 380 mm and a height of 400 mm. Ruston turbines with diameters of 128 mm were mounted in the tank. The off-bottom clearance of the lower impeller was

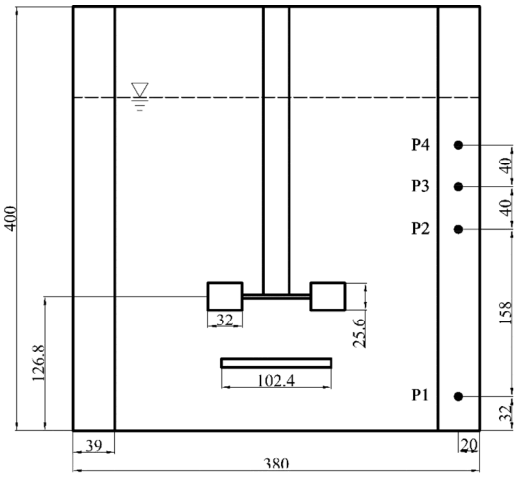

Figure 3 Schematic diagram of the stirred tank and locations of measurement points.

126.8 mm. The experiments were carried out at a constant temperature of 19 °C and ambient pressure. CO_2, which served as the dispersed gas phase, was introduced through a ring aerator with a diameter of 102.4 mm and 28 holes located between the tank base and the lower impeller. The [bmim][BF_4] served as the liquid phase. Its properties are summarized in Table 1. An impeller speed of 250 r/min and gas flow rates of 0.237, 0.356, 0.474, and 0.594 vvm were used. Because of the dense dispersion and internal shadows in the stirred tank, area photographs for use in characterizing the bubble size at axial positions were taken near the wall of tank [23].

3.2 Measurement technique

The mean bubble sizes at four different axial positions were determined using the image pick-up system. The bubbles were identified from ten pictures with resolutions of 1280 ×1024 pixels. At least 150 bubbles were selected for statistical analysis. The Sauter mean diameter (d_{32}) is defined as follows:

$$d_{32} = \frac{\sum_{i=1}^{N} d_i^3}{\sum_{i=1}^{N} d_i^2} \tag{21}$$

More detailed information on the process is provided in our previous work [13].

4 Results and discussion

4.1 Flow field

The flow configuration of the continuous phase generated by a single Ruston turbine is a very important aspect of the investigation of gas dispersion. For N=250 r/min, the liquid flow in an air-water system (Figure 4(a)) is pushed toward the wall of the tank by the radial impeller and eventually creates two circulation loops located on the upper and lower sides of the impeller. This flow pattern has been confirmed by many researchers [40,41]. Figure 4(b) shows that the mean velocity of the IL ([bmim][BF_4]) flow is lower than the velocity of the water flow field because of the former's much higher viscosity. Significant differences are detected in the size and position of the two circulation loops, which indicates that momentum transfer specific to water occurs easily, whereas for the IL, the influence of turbulent fluctuation is mainly concentrated in the zone near the impeller.

4.2 Gas holdup

The hydrodynamics of total and local gas holdup are considered to be key parameters in the flow regime in the stirred tank. The total gas holdup at various gas flow rates

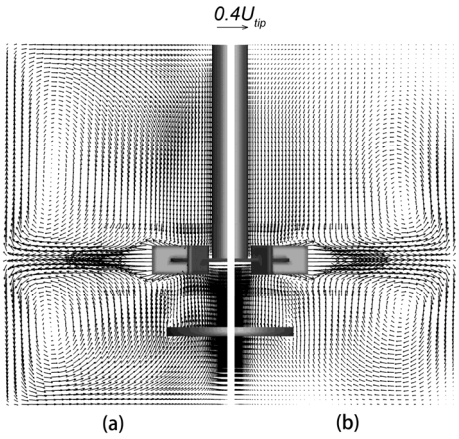

Figure 4 Predicted velocity vector profiles of single phase at mid baffle plane (U_{tip}=1.676 m/s). (a) Water; (b) [bmim][BF_4].

and an agitation speed of N=250 r/min was measured using a transparent tapeline attached to the tank wall. The measured values were confirmed to be efficient according to Paglianti *et al.* [42]. The total gas holdup can be calculated as follows:

$$\varphi_g = \frac{H_g - H}{H_g} \tag{22}$$

where φ_g is the total gas holdup, H is the ungassed liquid height (m), H_g is the liquid height after gas dispersion (m).

Satisfactory agreement was obtained between the predictions and experimental measurements, as shown in Table 2. Three factors contribute to the satisfactory agreement. First, the specific drag model for gas-IL system developed by Dong *et al.* [13] was applied to the current cases, where the dimensionless number Mo in Eq. (5) reflects the influence of the physical properties of the IL on interphase exchange. Second, the effect of bubble settling velocity reduction due to turbulence was considered by adding a drag factor proposed by Brucato *et al.* [32]. Third, the PBM describes the bubble size distribution at any point in the stirred tank, which is more realistic than the assumption of a constant bubble size. An example of local gas holdup based on numerical predictions for an agitation rate of 250 r/min and a gassing rate of 0.237 vvm is presented in Figure 5. Gas accumulates in both recirculation regions, although it is less obvious for the lower circulation loop, and bubbles rise toward the middle of the tank. Relatively large gas holdup occurs behind the blades because of the formation of gas cavities [41], whereas very few bubbles gather in the region under the impeller. Similar trends have been reported by Laakkonen *et al.* [23].

Figure 6 shows the effects of different operating conditions on the axial distribution of the local gas holdup at the radial position r=160 mm. The average local gas holdup in the axial direction can be expressed as follows:

$$\overline{\alpha_b} = 0.025V_g^{0.73} \quad R = 0.99 \tag{23}$$

$$\overline{\alpha_b} = 77.23T^{-0.28} \quad R = 0.92 \tag{24}$$

where V_g and T are the gas flow rate and temperature, respectively, and R is the correlation coefficient. The power values, positive or negative, represent the variation in the average local gas holdup with gassing rate and temperature.

The gas holdup increases dramatically and then decreases in the axial direction, with a peak located near the height of the impeller. Both the agitation speed and the gas flow rate have a positive influence on the local gas holdup. Compared with the gas flow rate, the agitation speed has a greater effect in intensifying the circulation of the flow field. Thus, the local gas holdup below the impeller increases considerably (Figure 6(b)). As Figure 6(c) shows, the local gas holdup exhibits a downward trend with increasing temperature. The possible reasons for this are as follows. As the temperature increases, the viscosity of [bmim][BF_4] decreases significantly, which can result in an increase in bubble size and a reduction in bubble residence time [43]. For the values of the peaks shown in Figure 6, an almost linear increasing tendency was observed. However, the increase shown in Figure 6(b) is much smaller than the others, which indicates a homogeneous dispersion of bubbles. Therefore, a higher gas flow rate and higher temperature are beneficial in terms of increasing the total gas holdup, and the quality of gas dispersion is also improved by a higher rotational speed.

Table 2 Comparison of experimental and predicted values of total gas holdup (N=250 r/min)

S. No.	Gas flow rate (vvm)	Total gas holdup	
		Experimental	Predicted
1	0.237	0.0127	0.0117
2	0.356	0.0159	0.0145
3	0.474	0.0190	0.0169
4	0.594	0.0222	0.0194

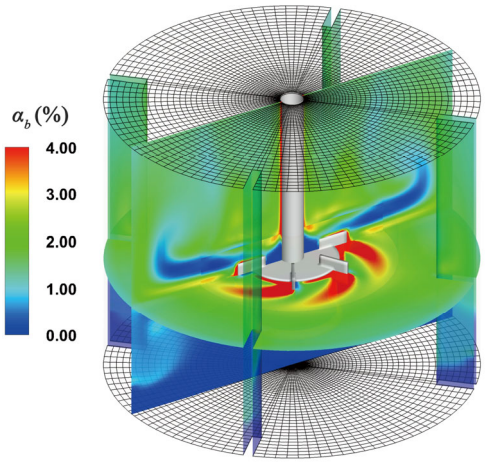

Figure 5 Predicted local gas holdup (%) in the case of agitation rate of 250 r/min and gas flow rate of 0.237 vvm on two vertical planes.

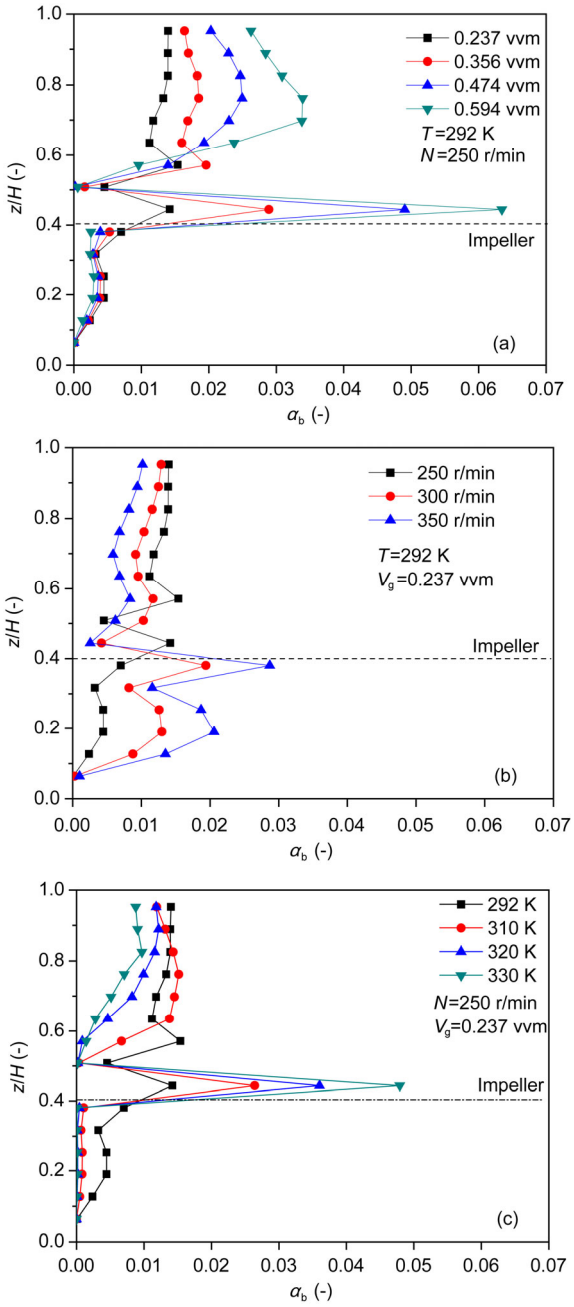

Figure 6 Predicted axial distributions of local gas holdup for different operating conditions.

4.3 Bubble size

Bubble size is another parameter that is important not only in evaluation of the mixing quality of a gas-liquid system in a stirred tank but also in providing a reference for further investigation of mass transfer between bubbles and liquids. The local Sauter diameter (d_{32}), which is equal to the ratio of moments of orders three and two, is illustrated in Figure

7. Large bubbles are found in the center of the vessel and the two circulation loops, where the bubble coalescence prevails. Along the turbine discharge streams, small bubbles are generated because of the relatively high bubble breakage rate. In addition, bubbles downwind of baffles are larger than bubbles upwind of baffles (Figure 8). This can be explained by the formation of stationary vortices downwind of baffles leading to bubble accumulation and bubble breakage playing a primary role on the other side of baffles [24,44]. Table 3 shows that the predicted values for d_{32} are consistent with the experimental data when the gas flow rate is 0.237 vvm. As the gassing rate increases, the predicted values become larger than the experimental values. This may be due to slight overestimation of the bubble coalescence rate using Eq. (14). Overall increasing trends in bubble size are presented for measuring points P2 to P4. However, the trend for point P1 is inconsistent with those other trends.

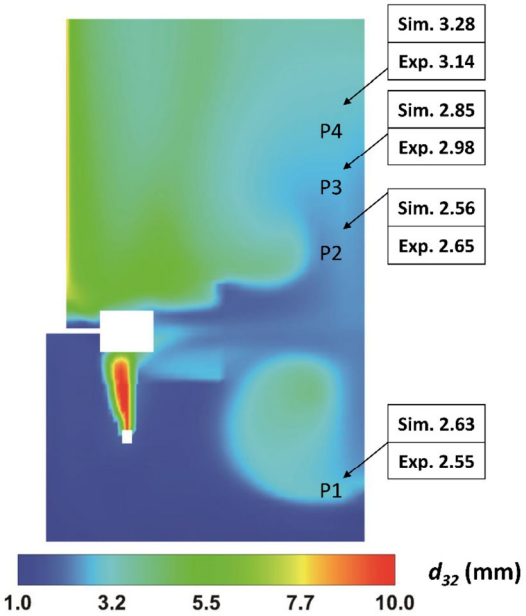

Figure 7 Local Sauter diameter (mm) distribution and comparisons between predictions and experimental data for axial planes at 250 r/min and 0.237 vvm.

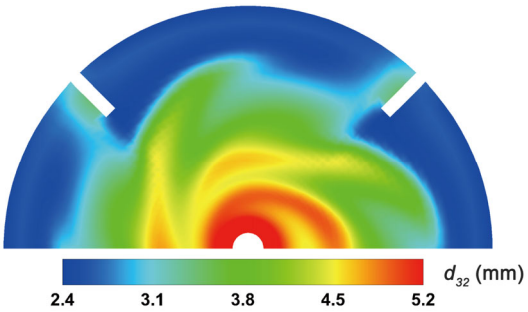

Figure 8 Local Sauter diameter (mm) distribution on a tangential plane at 250 r/min and 0.237 vvm.

Table 3 Comparisons of d_{32} between simulations and experimental results for the monitoring points

Gas flow rate (vvm)		P1	P2	P3	P4
0.237	Exp.	2.55	2.65	2.98	3.14
	Sim.	2.63	2.56	2.85	3.28
0.356	Exp.	2.26	2.91	3.20	3.58
	Sim.	2.56	2.87	3.13	3.57
0.474	Exp.	2.00	3.09	3.47	3.22
	Sim.	2.51	3.22	3.43	3.96
0.594	Exp.	2.16	3.90	3.62	4.19
	Sim.	2.46	3.51	3.63	4.29

The axial distributions of d_{32} at a radial position of r=126 mm under various conditions are shown in Figure 9. The broken lines for d_{32} vs. the dimensionless height illustrate a typical distribution along with the axial positions. It can be seen that the values of d_{32}, which are located below the upper circulation loop, are insensitive to increasing gassing rate at 250 r/min (Figure 9(a)). However, notable variations are detected in the regions of the impeller and the lower circulation loop (Figure 9(b, c)). For example, a 35% reduction in d_{32} in the turbine discharge region is observed for rotational speeds from 250 to 350 r/min. As a consequence, the physical properties of the IL and the agitation speed play key roles in both bubble breakage and bubble coalescence, while an increase in the gassing rate mainly increases the probability of bubble coalescence. It is noted that for the high viscosity (94.08 mPa s) of the liquid phase in the present system, a spherical bubble shape is maintained more stably than in a lower-viscosity system [11]. Moreover, according to Xing *et al.* [45], the bubble breakup rate decreases sharply when the liquid viscosity is higher than 10 mPa s. Therefore, the phenomenon of bubble coalescence prevails outside the impeller region, in comparison to bubble breakage.

4.4 Volumetric bubble size distribution

For gas-liquid systems in reactors, the quality of mass transfer is related to the mass transfer area. Compared with the assumption of an average bubble size, consideration of local BSDs is more efficient in describing the efficient mass transfer area. In this case, the predicted volumetric bubble size distribution is reconstructed from the moments, assuming a log-normal distribution, as described by John *et al.* [46]. The volume density function can be expressed as follows:

$$f(L)=\frac{n(L)L^3}{\int_0^\infty n(L)L^3\mathrm{d}L} \tag{25}$$

Figure 10 shows the local volumetric bubble size distributions at various locations in the stirred tank. The size

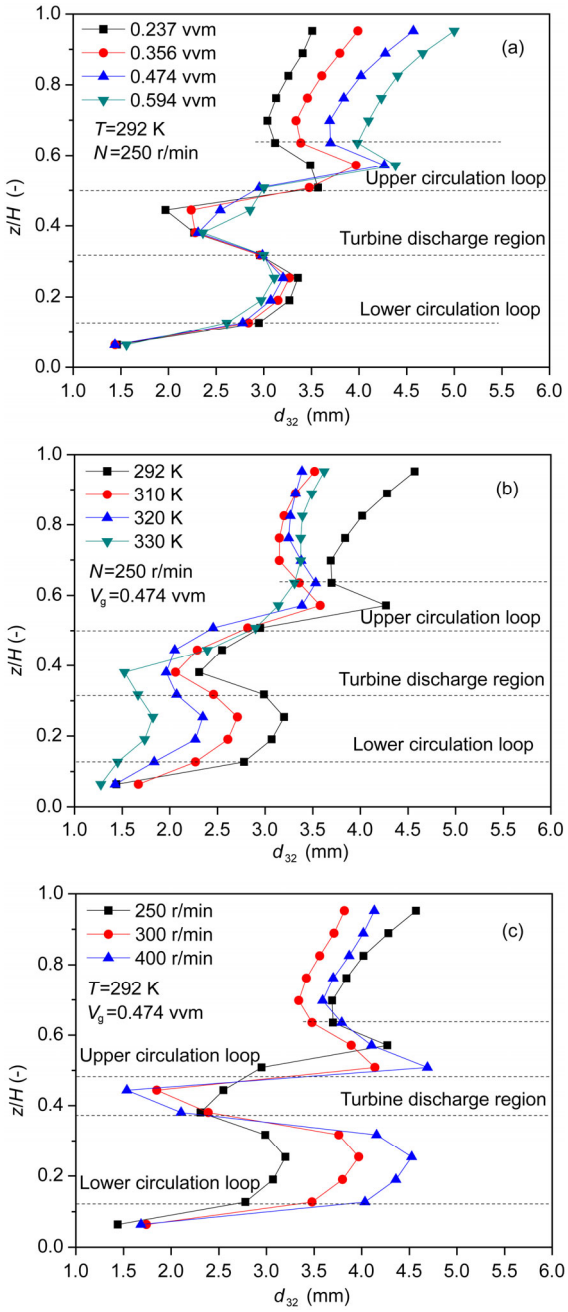

Figure 9 Predicted axial distributions of local Sauter diameter (d_{32}) for different operating conditions.

distribution widens toward the liquid surface and the center of the tank. Furthermore, the peak value of the bubble size distribution increases as the gassing rate increases, which indicates that bubble coalescence plays a dominant role. Along the turbine discharge flow (P5 (r=170 mm, z=126.8 mm)), large bubbles break up into small bubbles because of strong turbulent dissipation. However, at the position below the impeller (P1), the composition of the bubbles remains almost constant for various gassing rates. For positions P6 (r=64 mm, z=270 mm) and P7 (r=64 mm, z=230 mm), it is evident that the volumetric density is much lower than at P3

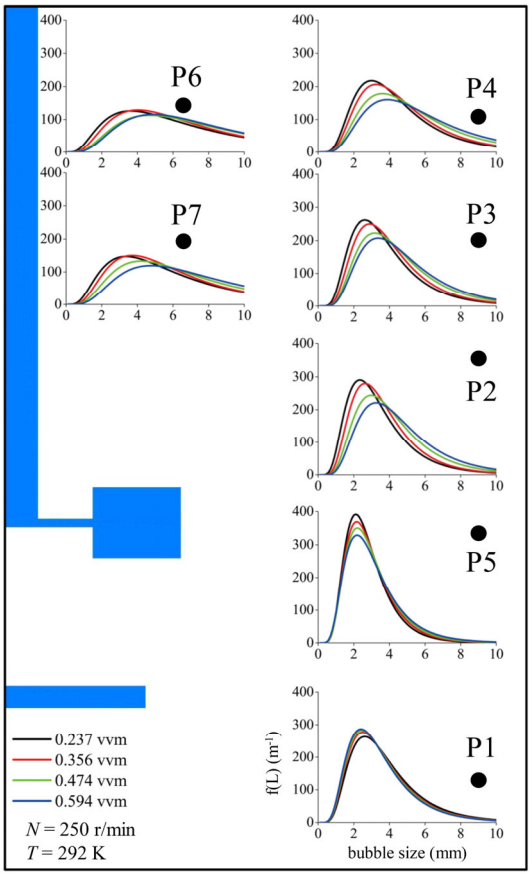

Figure 10 Local volumetric bubble size distributions for different gassing rates.

and P4. This can be explained as follows. At positions near the shaft, the gas phase accumulates, and the turbulence intensity is fairly low. This results in a large fraction of large bubbles and a small bubble breakage rate. Moreover, the intensity of the flow field decreases considerably as the gas holdup increases at P6 and P7. Therefore, viscous shear is much lower at locations close to the tank wall.

4.5 Interfacial area

The interfacial area is a vital parameter for describing mass transfer and gas-liquid reactor design. Based on the local Sauter diameter distribution and the local gas holdup value, the interfacial area can be calculated as follows:

$$a = \frac{6\alpha_b}{d_{32}} \tag{26}$$

where a is the interfacial area (m^2/m^3).

Figure 11 shows the axial distributions (r=126 mm) of interfacial areas for various gassing rates. Similar profiles were detected for the various gassing rates, and the peak values were detected just above the impeller, which is consistent with observations reported by Bao *et al.* [47]. As described in the preceding sections, the small bubble size

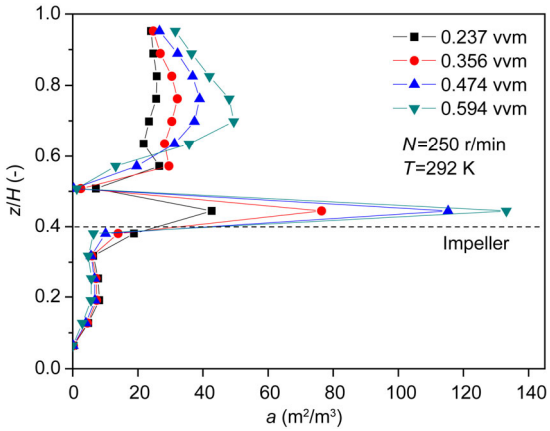

Figure 11 Predicted axial distributions of interfacial area for different gassing rates.

and relatively high gas holdup result in a sharp increase in the impeller region. At locations above the impeller region, because of the higher growth rate compared to the d_{32}, the gas holdup has a more positive effect on the interfacial area as the gassing rate increases.

5 Conclusions

In this study, a Eulerian multiphase model coupled with a PBM was used to simulate CO_2 dispersion in [bmim][BF_4] in a stirred tank. A new drag model specific to a gas-IL system, proposed in our previous work, was applied to describe the interaction between IL and bubbles of different sizes. The population balance equations used, which include parameters for bubble breakage and bubble coalescence, were solved by QMOM. The simulation results show good agreement with experimental data on gas holdup and the local Sauter diameter.

The bubble behavior in IL was investigated under a wide range of operating conditions. The results demonstrate that the total gas holdup increases with increasing gassing rate and agitation speed, while the local gas holdup decreases with increasing temperature. The bubble breakage rate is low in [bmim][BF_4] because of the high viscosity of the IL. The physical properties of the IL and the agitation speed affect both bubble breakage and bubble coalescence, while higher gassing rates mainly increase the probability of bubble coalescence. In the region above the impeller, large bubbles are generated due to the increasing bubble coalescence rate.

This numerical approach may serve as a robust basis for research on mass transfer between gas and ILs. The results obtained for the range of operating conditions considered suggest that a rotational speed of 350 r/min, a gas flow rate of 0.594 vvm, and a temperature of 292 K are beneficial for absorption.

This work was supported by the National Natural Science Fund for Distinguished Young Scholars (21425625), the National Natural Science Foundation of China (21436010, 21376242), and the Key Program of the Beijing Municipal Natural Science Foundation (2141003).

1 Hallett JP, Welton T. Room-temperature ionic liquids: solvents for synthesis and catalysis. 2. *Chem Rev*, 2011, 111: 3508–3576
2 Dupont J, de Souza RF, Suarez PA. Ionic liquid (molten salt) phase organometallic catalysis. *Chem Rev*, 2002, 102: 3667–3692
3 Li X, Zhao D, Fei Z, Wang L. Applications of functionalized ionic liquids. *Sci China Chem*, 2006, 49: 385–401
4 Zhang X, Zhang X, Dong H, Zhao Z, Zhang S, Huang Y. Carbon capture with ionic liquids: overview and progress. *Energy Environ Sci*, 2012, 5: 6668–6681
5 Zhang S, Zhang X, Zhao Y, Zhao G, Yao X, Yao H. A novel ionic liquids-based scrubbing process for efficient CO_2 capture. *Sci China Chem*, 2010, 53: 1549–1553
6 Kolding H, Fehrmann R, Riisager A. CO_2 capture technologies: current status and new directions using supported ionic liquid phase (silp) absorbers. *Sci China Chem*, 2012, 55: 1648–1656
7 Zhang Z, Hu S, Song J, Li W, Yang G, Han B. Hydrogenation of CO_2 to formic acid promoted by a diamine-functionalized ionic liquid. *ChemSusChem*, 2009, 2: 234–238
8 Sun J, Cheng W, Fan W, Wang Y, Meng Z, Zhang S. Reusable and efficient polymer-supported task-specific ionic liquid catalyst for cycloaddition of epoxide with CO_2. *Catal Today*, 2009, 148: 361–367
9 Sun J, Zhang S, Cheng W, Ren J. Hydroxyl-functionalized ionic liquid: a novel efficient catalyst for chemical fixation of CO_2 to cyclic carbonate. *Tetrahedron Lett*, 2008, 49: 3588–3591
10 Zhang S, Sun J, Zhang X, Xin J, Miao Q, Wang J. Ionic liquid-based green processes for energy production. *Chem Soc Rev*, 2014, 43: 7838–7869
11 Zhang X, Dong H, Bao D, Huang Y, Zhang X, Zhang S. Effect of small amount of water on CO_2 bubble behavior in ionic liquid systems. *Ind Eng Chem Res*, 2013, 53: 428–439
12 Zhang X, Dong H, Huang Y, Li C, Zhang X. Experimental study on gas holdup and bubble behavior in carbon capture systems with ionic liquid. *Chem Eng J*, 2012, 209: 607–615
13 Dong H, Wang X, Liu L, Zhang X, Zhang S. The rise and deformation of a single bubble in ionic liquids. *Chem Eng Sci*, 2010, 65: 3240–3248
14 Kaji R, Zhao D, Licence P, Azzopardi BJ. Studies of the interaction of ionic liquid and gas in a small-diameter bubble column. *Ind Eng Chem Res*, 2009, 48: 7938–7944
15 Torres-Martínez D, Melgarejo-Torres R, Gutiérrez-Rojas M, Aguilera-Vázquez L, Micheletti M, Lye GJ, Huerta-Ochoa S. Hydrodynamic and oxygen mass transfer studies in a three-phase (air-water-ionic liquid) stirred tank bioreactor. *Biochem Eng J*, 2009, 45: 209–217
16 Khopkar AR, Kasat GR, Pandit AB, Ranade VV. CFD simulation of mixing in tall gas-liquid stirred vessel: role of local flow patterns. *Chem Eng Sci*, 2006, 61: 2921–2929
17 Khopkar AR, Tanguy PA. CFD simulation of gas-liquid flows in stirred vessel equipped with dual rushton turbines: influence of parallel, merging and diverging flow configurations. *Chem Eng Sci*, 2008, 63: 3810–3820
18 Ranade V, van den Akker H. A computational snapshot of gas-liquid flow in baffled stirred reactors. *Chem Eng Sci*, 1994, 49: 5175–5192
19 Bartels C, Breuer M, Wechsler K, Durst F. Computational fluid dynamics applications on parallel-vector computers: computations of stirred vessel flows. *Comput Fluids*, 2002, 31: 69–97
20 Hartmann H, Derksen J, Montavon C, Pearson J, Hamill I, van den Akker H. Assessment of large eddy and rans stirred tank simulations by means of LDA. *Chem Eng Sci*, 2004, 59: 2419–2432

21 Lane GL, Schwarz MP, Evans GM. Numerical modelling of gas-liquid flow in stirred tanks. *Chem Eng Sci*, 2005, 60: 2203–2214
22 Kerdouss F, Bannari A, Proulx P. CFD modeling of gas dispersion and bubble size in a double turbine stirred tank. *Chem Eng Sci*, 2006, 61: 3313–3322
23 Laakkonen M, Moilanen P, Alopaeus V, Aittamaa J. Modelling local bubble size distributions in agitated vessels. *Chem Eng Sci*, 2007, 62: 721–740
24 Petitti M, Nasuti A, Marchisio DL, Vanni M, Baldi G, Mancini N, Podenzani F. Bubble size distribution modeling in stirred gas-liquid reactors with qmom augmented by a new correction algorithm. *AIChE J*, 2010, 56: 36–53
25 Venneker BC, Derksen JJ, van den Akker HE. Population balance modeling of aerated stirred vessels based on CFD. *AIChE J*, 2002, 48: 673–685
26 Muhr H, David R, Villermaux J, Jezequel P. Crystallization and precipitation engineering-VI. Solving population balance in the case of the precipitation of silver bromide crystals with high primary nucleation rates by using the first order upwind differentiation. *Chem Eng Sci*, 1996, 51: 309–319
27 McGraw R. Description of aerosol dynamics by the quadrature method of moments. *Aerosol Sci Tech*, 1997, 27: 255–265
28 Marchisio DL, Vigil RD, Fox RO. Quadrature method of moments for aggregation-breakage processes. *J Colloid Interf Sci*, 2003, 258: 322–334
29 Marchisio DL, Vigil RD, Fox RO. Implementation of the quadrature method of moments in CFD codes for aggregation-breakage problems. *Chem Eng Sci*, 2003, 58: 3337–3351
30 Wang X, Dong H, Zhang X, Xu Y, Zhang S. Numerical simulation of absorbing CO_2 with ionic liquids. *Chem Eng Technol*, 2010, 33: 1615–1624
31 Wang X, Dong H, Zhang X, Yu L, Zhang S, Xu Y. Numerical simulation of single bubble motion in ionic liquids. *Chem Eng Sci*, 2010, 65: 6036–6047
32 Brucato A, Grisafi F, Montante G. Particle drag coefficients in turbulent fluids. *Chem Eng Sci*, 1998, 53: 3295–3314
33 Marchisio DL, Fox RO. *Computational Models for Polydisperse Multiphase Flows*. Cambridge: Cambridge University Press, 2013
34 Luo H, Svendsen HF. Theoretical model for drop and bubble breakup in turbulent dispersions. *AIChE J*, 1996, 42: 1225–1233
35 Coulaloglou C, Tavlarides L. Description of interaction processes in agitated liquid-liquid dispersions. *Chem Eng Sci*, 1977, 32: 1289–1297
36 Prince MJ, Blanch HW. Bubble coalescence and break-up in air-sparged bubble columns. *AIChE J*, 1990, 36: 1485–1499
37 Zhang X, Bao D, Huang Y, Dong H, Zhang X, Zhang S. Gas-liquid mass-transfer properties in CO_2 absorption system with ionic liquids. *AIChE J*, 2014, 60: 2929–2939
38 Sánchez LG, Meindersma G, De Haan A. Kinetics of absorption of CO_2 in amino-functionalized ionic liquids. *Chem Eng J*, 2011, 166: 1104–1115
39 Gordon RG. Error bounds in equilibrium statistical mechanics. *J Math Phys*, 1968, 9: 655–663
40 Lane GL, Schwarz MP, Evans GM. Predicting gas-liquid flow in a mechanically stirred tank. *Appl Math Model*, 2002, 26: 223–235
41 Murthy BN, Ghadge RS, Joshi JB. CFD simulations of gas-liquid-solid stirred reactor: prediction of critical impeller speed for solid suspension. *Chem Eng Sci*, 2007, 62: 7184–7195
42 Paglianti A, Takenaka K, Bujalski W, Takahashi K. Estimation of gas hold-up in aerated vessels. *Can J Cheml Eng*, 2000, 78: 386–392
43 Gao Z, Smith JM, Müller-Steinhagen H. Void fraction distribution in sparged and boiling reactors with modern impeller configuration. *Chem Eng Process*, 2001, 40: 489–497
44 Buffo A, Vanni M, Marchisio DL. Multidimensional population balance model for the simulation of turbulent gas-liquid systems in stirred tank reactors. *Chem Eng Sci*, 2012, 70: 31–44
45 Xing C, Wang T, Wang J. Experimental study and numerical simulation with a coupled CFD-PBM model of the effect of liquid viscosity in a bubble column. *Chem Eng Sci*, 2013, 95: 313–322
46 John V, Angelov I, Öncül A, Thévenin D. Techniques for the reconstruction of a distribution from a finite number of its moments. *Chem Eng Sci*, 2007, 62: 2890–2904
47 Bao Y, Chen L, Gao Z, Chen J. Local void fraction and bubble size distributions in cold-gassed and hot-sparged stirred reactors. *Chem Eng Sci*, 2010, 65: 976–984